Powder Technology 407 (2022) 117607

Contents lists available at ScienceDirect

Powder Technology

journal homepage: www.journals.elsevier.com/powder-technology

Modelling the tribocharging process in 2D and 3D

J.N. Rasera [a,b,*], R.D. Cruise [a], J.J. Cilliers [a], J.-A. Lamamy [b], K. Hadler [a]

[a] Imperial College London, Dept. Earth Sciences and Engineering, Exhibition Road, London SW7 2AZ, United Kingdom
[b] ispace Europe S.A., 5, rue de l'Industrie, L-1811 Luxembourg

HIGHLIGHTS

- Tribocharging models often depend on ill-defined or poorly quantified parameters.
- An effective empirical model parameter evaluation method is presented and validated.
- The efficacy of 2D/3D DEM models using these parameters is compared and evaluated.
- 2D and 3D models simulate successfully tribocharging due to single contacts.
- Only 3D models agree experimental data in complex (multi-particle/contact) systems.

GRAPHICAL ABSTRACT

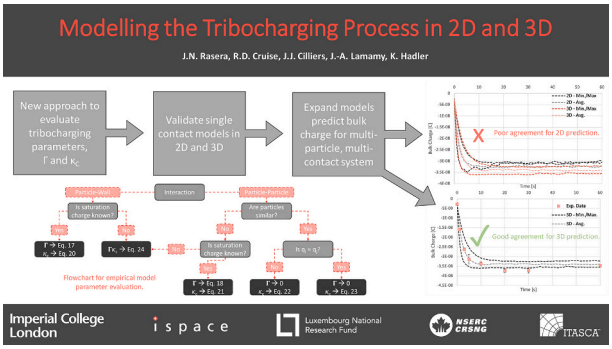

ARTICLE INFO

Keywords:
Tribocharge modelling
Discrete element method (DEM)
Electrostatic processes
Computational electrostatics

ABSTRACT

Many discrete element method (DEM) tribocharging models presented in the literature rely on ill-defined or poorly quantified charging parameters. This work presents a straightforward experimental method to quantify key parameters, namely the charge transfer limit, Γ, and the charging efficiency, κ_c. These parameters are then used in both 2D and 3D DEM simulations to evaluate the applicability of faster 2D models to tribocharge modelling. Both the 2D and 3D models are found to perform well against the experimental data for single-contact and single-particle, multi-contact systems. However, the 2D model fails to produce good agreement with experimental data for multi-contact, multi-particle systems. This approach for determining experimentally the parameters for the DEM tribocharging model is found to be effective and produces good agreement between simulated and experimental data. This method will improve and simplify the DEM modelling of triboelectric charging in dry material handling processes.

1. Introduction

Tribocharging is a method of imparting charge by frictional contact. This process occurs through the exchange of discrete quantities of charge as objects come into contact with other objects or their surroundings. The magnitude of tribocharging is dependent on many factors, such as humidity, ambient temperature, impact velocity, flow density, and material composition [1,2]. Tribocharging can be an unwanted process for which mitigation is required, or can be exploited to separate materials with different surface charging properties [1]. Tribocharging has been observed for millennia [3], however many of the

* Corresponding author.
E-mail address: j.rasera@imperial.ac.uk (J.N. Rasera).

https://doi.org/10.1016/j.powtec.2022.117607
Received 26 April 2022; Received in revised form 3 June 2022; Accepted 4 June 2022
Available online 12 June 2022

Nomenclature

$\ddot{x}$	Translational acceleration
$\vec{a}$	Translational acceleration
$\vec{F}_{\text{net}}$	Net force
m	Mass
$\vec{g}$	Acceleration due to gravity
i	Particle i
j	Particle j
$\vec{F}_c$	Local contact force
$\vec{F}_e$	Electrostatic force
$\vec{F}_a$	Applied force
$\vec{F}_h$	Non-linear Hertz force
$\vec{F}_d$	Dashpot force
$\vec{M}_c$	Moment at the point of contact
δ_c	Contact gap
n	Normal component
h	Hertz
d	Dashpot
*	Effective value, evaluated from two interacting particles
Y	Young's modulus
r	Radius
ν	Poisson's ratio
G	Shear modulus
s	Shear component
0	Indicates value at beginning of timestep
μ	Coefficient of friction
β	Damping coefficient
$\vec{v}_{\text{ij}}$	Relative velocity
ρ	Density
t	Time
Δt_{crit}	Critical timestep
σ	Surface charge density
φ	Effective work function
δ_e	Charge transfer cutoff distance
κ_c	Charging efficiency
ε_0	Permittivity of free space
e	Electron charge magnitude
$\vec{E}$	Electric field strength
$\hat{n}$	Unit normal vector
q	Charge
A	Area
ΔA	Change in contact area
Δq	Change in charge
Γ	Charge transfer limitation parameter
sat	Saturation
σ_f	Saturation charge density of an infinite plane
Φ	Surface potential difference
$\hat{r}$	Radial unit vector
$\vec{x}$	Position
r_{cutoff}	Strong interaction cutoff radius
n	Number of particles within the domain
ρ_q	Area/Volumetric charge density
m	Number of computational cells

physical mechanisms underpinning it are poorly understood [4–6]. While the empirically-derived triboelectric series indicates the charge polarities resulting from an interaction, determining the magnitude of charge transferred is nontrivial. Semi-empirical tribocharging models based on contact mechanics and surface state theory show good agreement with experimental data [7–9]. Practically, however, their use is often limited to simple interactions between a few particles under controlled and well-instrumented conditions. This is because the interaction mechanics between two or more objects are dependent on factors such as relative velocity, preexisting surface charge, and the local electrostatic field. These quantities are not known typically in real-time, especially for complex systems with hundreds, if not thousands, of interactions per second.

To address these experimental limitations, many workers have employed a variety of numerical approaches to model and understand the tribocharging process [3,10–23]. One approach of particular interest is the application of Cundall and Strack's [24,25] discrete element method (DEM) to tribocharging [13–21]. The underlying principle of the DEM lends itself to coupling with tribocharging models, as critical charge transfer parameters (e.g., contact area, relative velocity) are extracted easily. Laurentie et al. [13,14] implemented charging models proposed by Ali et al. [18] and Schein et al. [26] in a 2D-DEM model to study the tribocharging of polyamide (PA) and polycarbonate (PC) particles in a vibrating bed. The authors found good agreement with their experimental data, however their chosen approach necessitated the use of artificial limits on the maximum charge for a given species. Further, their model was dependent on a self-described "guess and try" approach to determine key model parameters. Kolehmainen et al. [15–17] extended the work of Laurentie et al. to couple 3D CFD and DEM models for pneumatically-conveyed particles using LIGGGHTS and OpenFOAM, and developed a novel approach to evaluating contributions from long-range electrostatic fields based on the solution of Poisson's equation for electrostatics. While these authors have demonstrated successfully the use of the DEM for modelling triboelectric charging, the models are dependent on poorly quantified or ill-defined parameters, such as an effective work function for insulating materials. Konopka and Kosek [21] present an alternative approach for particle-particle charge transfer that employs the exchange of discrete transferable charge species (electrons or ions) between contacting particles. While this method eliminates parameters like the work function and contributes greatly to the understanding of charge distribution in granular systems, it does not extend to particle-wall interactions [21]. Furthermore, these studies have focused on either 2D or 3D simulations. The benefits and limitations of modelling in 2D versus 3D have not been considered explicitly with respect to tribocharging.

The objectives of this work are threefold: the first is to introduce a method for quantifying key model parameters from experimental data; the second is to determine charge transfer for a single species system containing multiple particles with a view to designing effective tribochargers; and the third is to evaluate the performance of tribocharging models in 2D and 3D. In Section 2 of this article, we introduce the mathematical models and charging model parameters. We then present a straightforward approach for determining key model parameters for particle-wall and particle-particle contacts from experimental data to eliminate poorly defined constants. We then discuss the implementation of the models in Matlab (2D) and Itasca International's Particle Flow Code (PFC; 3D). Section 3 discusses the performance of the models for single-contact particle-wall and particle-particle interactions against published data from the literature. Section 4 describes the experimental techniques employed for both extracting the model parameters and generating charge data to validate the models for multi-contact and multi-particle scenarios. In Section 5, we extend the model to multiple contacts and multiple particles, and compare the performance to experimental data.

2. Mathematical models

An aim of this work is to determine if complex 3D models are necessary for modelling triboelectrification, or if simplified 2D models can be used. The use of 2D models is attractive from a computational efficiency perspective, as both the number of particles and degrees of freedom are restricted compared to an equivalent 3D geometry. However, the extent of the differences in the reliability of results from 2D and 3D models is unclear. To our knowledge, there have been no previous studies directly comparing the outputs of 2D and 3D DEM tribocharging models.

The 2D DEM solver was built in-house using Matlab. The 3D model was developed using Itasca International's PFC software. While PFC is a purpose-built DEM solver, it does not offer native triboelectric charge modelling capabilities. Hence, a tribocharging model was written with Python and implemented in PFC. It should be noted that the models described herein are applicable to single-particle/single-contact interactions as well as to multi-particle/multi-contact systems in 2- and 3D.

2.1. Mechanical

The DEM was developed by Cundall and Strack [24] for the simulation and analysis of rock mechanics and impacts. The method was then applied subsequently to the study of soil mechanics [25]. Thorough overviews of the DEM are provided by Cundall and Strack [27] and Hart [28]; a brief overview is provided here for completeness.

Particle interactions are treated as dynamic processes in the DEM. Contact forces and relative displacements are evaluated by tracking the motion of individual particles. Over each timestep, particle accelerations and velocities are kept constant. Discrete element models employ Newton's second law of motion and a force-displacement relationship to evaluate particle interactions, forces and motion. Integrating Newton's law once provides relative particle motion characteristics, and integrating a second time solves for particle positions. The force-displacement method selected determines the way that contact forces are evaluated and applied to each contact [29].

The translational acceleration, $\ddot{\vec{x}}_i$, of particle i is found by rearranging Newton's second law:

$$\ddot{\vec{x}}_i = \vec{a}_i = \frac{\vec{F}_{\text{net}}}{m_i} + \vec{g}, \tag{1}$$

where m_i is the mass of the particle, and $\vec{g}$ is the acceleration due to gravity. $\vec{F}_{\text{net}}$ is the sum of the forces acting on the particle, given by:

$$\vec{F}_{\text{net}} = \vec{F}_c + \vec{F}_e + \vec{F}_a, \tag{2}$$

where $\vec{F}_c$ is the local contact force, $\vec{F}_e$ is the electrostatic force, and $\vec{F}_a$ is any externally applied force. The equations of translational motion are solved using a second-order Velocity Verlet algorithm (Fig. 1).

Following, Laurentie et al. [13,14], Kolehmainen et al. [15–17], and others (e.g., [18,19,31,32]), we employ the Hertz-Mindlin force-displacement model whereby particle stiffness is assumed to be nonlinear. Further, the Hertz-Mindlin approach considers both normal and shear force components compared to the linear/Hooke approach that considers only the normal component. It should be noted that all particles are assumed to interact elastically and plastic deformation is not considered.

The Hertz-Mindlin contact model is applied to each particle-particle and particle-wall interaction. Thus, $\vec{F}_c$ is evaluated by:

$$\vec{F}_c = \vec{F}_h + \vec{F}_d \tag{3}$$

where $\vec{F}_h$ is the nonlinear Hertz force (Fig. 2a) and $\vec{F}_d$ is the dashpot force (Fig. 2b). Both the Hertz and dashpot forces are resolved subsequently into their normal and shear components in the coordinate system of the contact plane. In the Hertz-Mindlin model, the contact interface allows for rotational motion of particles, hence the moment at the point of contact is zero ($\vec{M}_c \equiv 0$).

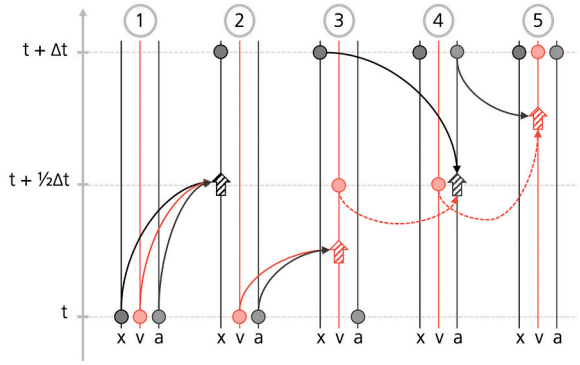

Fig. 1. Overview of the second order Velocity Verlet algorithm, adapted from Holm [30]. 1. Start from initial position. 2. Determine the new particle position by $\vec{x}(t+\Delta t) = \vec{x}(t) + \vec{v}(t)\Delta t + 0.5\vec{a}(t)\Delta t^2$. 3. Evaluate the velocity at $t + \Delta t/2$ by $\vec{v}(t+0.5\Delta t) = \vec{v}(t) + 0.5\vec{a}(t)\Delta t$. 4. Determine the acceleration from the body forces, as shown in Eq. (1). 5. Find the new velocity by $\vec{v}(t+0.5\Delta t) = \vec{v}(t+0.5\Delta t) + 0.5\vec{a}(t+0.5\Delta t)\Delta t$.

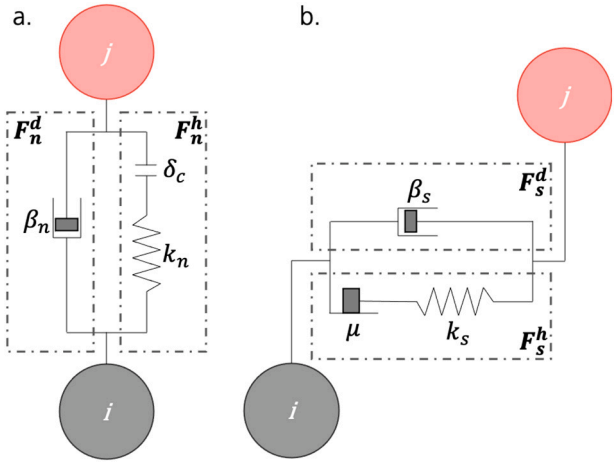

Fig. 2. Graphical overview of the force models for the normal direction (a) and the shear direction (b). Adapted from Laurentie et al. and Itasca CG [13,14,29].

The algorithms by which contact forces are evaluated are the same in both 2- and 3D. The logic is presented in detail by Itasca [29], and is summarised here:

1. Evaluate and update the Hertz normal force such that:

$$F_n^h = \begin{cases} \frac{4}{3} Y^* \sqrt{r^*}\, \delta_c^{3/2}, & \text{if } \delta_c \le 0.0 \\ 0.0, & \text{otherwise} \end{cases} \tag{4}$$

where δ_c is the contact gap extracted from the relative particle positions (which will be negative if contact is active). The effective contact radius, r^*, and the effective modulus of elasticity, Y^*, are given by:

$$r^* = \begin{cases} \frac{r_i r_j}{r_i + r_j}, & \text{if particle} - \text{particle}, \\ r_i, & \text{if particle} - \text{wall}, \end{cases} \tag{5}$$

and,

$$Y^* = \left(\frac{1-\nu_i}{2G_i} + \frac{1-\nu_j}{2G_j}\right)^{-1}, \tag{6}$$

respectively, where ν is Poisson's ratio and G is the shear modulus. Note that throughout this work, the subscripts i and j denote particle i or j in the system. In the case of a particle-wall contact, j refers to the wall.

2. Update the Hertz shear force:

$$\vec{F}_s^h = \begin{cases} \vec{F}_s^*, & \text{if } ||\vec{F}_s^*|| \le \mu F_n^h, \\ \mu F_n^h \dfrac{\vec{F}_s^*}{||\vec{F}_s^*||}, & \text{otherwise}, \end{cases} \tag{7}$$

where μ is the minimum coefficient of friction between the two particles, and $\vec{F}_s^*$ is an initial estimate of the shear force [29], given by:

$$\vec{F}_s^* = (\vec{F}_s^h)_0 - 8G^*\sqrt{r^*\delta_c}, \tag{8}$$

where $(\vec{F}_s^h)_0$ is the shear force at the beginning of the timestep. If the magnitude of the Hertz shear is equal to the friction force, μF_n^h, then it is assumed that the contact is slipping.

3. Update the dashpot normal force:

$$F_n^d = 2\sqrt{\frac{5}{6}}\beta\sqrt{2m^*Y^*\sqrt{r^*\delta_c}}\,\vec{v}_{ij}^n, \tag{9}$$

where β is the damping ratio, $\vec{v}_{ij}^n$ is the relative velocity in the normal direction, and m^* is the effective contact mass, given by:

$$m^* = \begin{cases} \dfrac{m_i m_j}{m_i + m_j}, & \text{if particle} - \text{particle}, \\ m_i, & \text{if particle} - \text{wall}. \end{cases} \tag{10}$$

4. Update the dashpot shear force:

$$\vec{F}_s^d = \begin{cases} 2\sqrt{\frac{5}{6}}\beta\sqrt{8m^*G^*\sqrt{r^*\delta_c}}\,\vec{v}_{ij}^s, & \text{if slipping}, \\ 0, & \text{otherwise}, \end{cases} \tag{11}$$

where $\vec{v}_{ij}^s$ is the relative velocity in the shear direction, and G^* is the effective shear modulus, given by:

$$G^* = \left(\frac{2-\nu_i}{G_i} + \frac{2-\nu_j}{G_j}\right)^{-1} \tag{12}$$

With regard to choice of timestep, different methods were employed for the 2D and 3D cases. For the 3D model, PFC automatically updates the timestep at the start of each calculation cycle to ensure the stability of the analytical solution. For the 2D model, a more simplistic fixed timestep based on the Rayleigh wave speed is used. The timestep is calculated following the method of Li et al. [33]:

$$\Delta t_{\text{crit}} = \frac{\pi r\sqrt{\rho/G}}{0.8766 + 0.163\nu} \tag{13}$$

Following the suggestion of Boac et al. [34], 20% of this value was used to ensure solution stability.

2.2. Tribocharging

The tribocharging model employed here follows that used by Laurentie et al. [13,14] and Kolehmainen et al. [15–17]. The model uses the high-density limit of surface state theory to describe the charge transferred between two surfaces [13,14,26,35], and is given by:

$$\sigma = \kappa_c\varepsilon_0\left(\frac{\varphi_i - \varphi_j}{\delta_e e} - \vec{E}_{\text{contact}}\cdot\hat{n}_{ij}\right) \tag{14}$$

In Eq. (14), σ is the charge transferred per unit area; κ_c is the empirically-derived charging efficiency; ε_0 is the permittivity of free space; δ_e is the separation distance between two particles at which point charge transfer ceases; e is the magnitude of the electron charge; φ_i and φ_j are the effective work functions; $\vec{E}_{\text{contact}}$ is the electrostatic field at the point of contact; and, $\hat{n}_{ij}$ is the unit normal vector pointing from particle i to j at the point of contact.

This expression can be re-written in terms of charge transferred, Δq, as a function of the change in contact area during a collision, ΔA:

$$\Delta q = \Delta A\kappa_c\varepsilon_0\left(\frac{\varphi_i - \varphi_j}{\delta_e e} - \vec{E}_{\text{contact}}\cdot\hat{n}_{ij}\right) \tag{15}$$

The form of Eq. (15) makes it suitable for implementation in a DEM system, as the evaluation of ΔA becomes trivial. From Hertzian theory, the contact area between two spheres, or between a sphere and a half-plane, can be approximated by $A = \pi r^*\delta_c$ [13,14]. By tracking the contact area at each timestep, ΔA is simply the difference in area between the current and previous timestep.

There are two fundamental challenges associated with Eqs. (14) and (15). The first is that the concept of an effective work function is not physically meaningful for insulating materials. In order to have an effective work function, thermodynamic equilibrium must be reached between the surface states [26]. However, as insulators naturally do not facilitate the movement of charge, it is unclear as to how equilibrium could be reached [26].

The second issue resides in the δ_e term. According to Harper [36], the value of δ_e should be on the order of 1 *nm*. When effective work function values from the literature are employed to evaluate δ_e, however, the results are often several orders of magnitude larger [26]. Lowel and Rose-Innes [37] report that using "plausible" values for δ_e (i.e., values on the order of several *nm*, in line with Harper) result in surface charge densities beyond what have been observed experimentally. Further, the "true" value of δ_e is sensitive to environmental conditions, such as ambient humidity, temperature and pressure, as well as the species participating in the exchange of charge [20]. Laurentie et al. employ a value of 500 *nm* in their model, and state that this is a "typical" value [13,14], however the origin of this value is unclear. Others (e.g., [16,17]) have since reused this value in their models.

To address both issues, we follow a similar approach to that suggested by Schein et al. and Sippola et al. [20,26], and introduce a lumped term, Γ, that we refer to as the charge transfer limitation parameter, as follows:

$$\Delta q = \Delta A\kappa_c\varepsilon_0\left(\Gamma - \vec{E}_{\text{contact}}\cdot\hat{n}_{ij}\right). \tag{16}$$

Employing a lumped parameter approach offers several advantages over the use of work functions and charge transfer distances. The first advantage is the minimisation of the significance of any one poorly-defined parameter. Another advantage is that Γ may be thought of as the electrostatic field required to drive the charge transfer to 0. This allows for the evaluation of Γ for a number of different material interactions using relatively simple experiments, or published data (if available). Finally, there are use cases for triboelectric charge modelling, such as the electrostatic beneficiation of minerals, where the work functions for certain particle species may have not yet been quantified.

Consider the limiting case of a single particle-wall system where the particle has attained its saturation charge, q_{sat}. The saturation charge is dependent on particle and wall materials, as well as the environmental conditions (temperature, humidity [1,2]), and the local electrostatic environment. Here, $\Delta q = 0$, hence Eq. (16) may be rearranged:

$$\Gamma = \vec{E}_{\text{contact}} \cdot \hat{n}_{\text{ij}} = \frac{q_{i,\text{sat}}}{4\pi\varepsilon_0 r_i^2} = \frac{\sigma_{i,\text{sat}}}{\varepsilon_0}, \tag{17}$$

where $\sigma_{i,sat}$ is the experimentally derived surface charge density at saturation. For particle-particle contacts:

$$\Gamma = \frac{\sigma_{i,\text{sat}} - \sigma_{j,\text{sat}}}{\varepsilon_0}, \tag{18}$$

noting that Γ tends to zero when particles are similar. The charge transfer limitation parameter is dependent on electrostatic parameters and particle size only, and is independent of particle kinematics and contact area.

By evaluating $\sigma_{i,sat}$ for at least two different particle sizes, the value of $\sigma_{i,sat}$ for a further size class may be approximated with the following relationship proposed by Cruise et al. [38]:

$$\sigma_{i,\text{sat}} = \frac{\sigma_f}{\varepsilon_0} + \frac{\Phi_{\text{sat}}}{r_i}, \tag{19}$$

where σ_f is the saturation charge density of an infinite plane, and Φ_{sat} is the surface potential at saturation.

Both σ_f and Φ_{sat} are assumed to be constant across all size fractions. This model can be used to provide a reasonable prediction for the saturation charge density of other particle sizes.

The charging efficiency term, κ_c, appears regularly in theoretical and experimental discussions of triboelectric charging (e.g, [35,39,40]). In previous works that modelled the tribocharging process using a DEM model (e.g., [13–17]), however, κ_c is omitted. In contrast, we find that the charging efficiency has a strong influence on the charging behaviour. This term must also be evaluated empirically. The calculation of κ_c is dependent on the mode of interaction (particle-particle vs particle-wall) as well as the particle size and contact area.

For particle-wall contacts, Eq. (17) is substituted into Eq. (16), and then rearranged to produce:

$$\kappa_c = \frac{4\pi r^2 \Delta q}{\Delta A (q_{i,\text{sat}} - q_i)}, \tag{20}$$

Eq. (20) can be written for dissimilar particle-particle contacts as:

$$\kappa_c = \frac{4\pi r_i^2 r_j^2 \Delta q}{\Delta A [r_j^2 (q_{i,\text{sat}} - q_i) - r_i^2 (q_{j,\text{sat}} - q_j)]}, \tag{21}$$

and for similar particles as:

$$\kappa_c = \frac{4\pi r^2 \Delta q}{\Delta A (q_j - q_i)}. \tag{22}$$

When two particles have similar charges, such that $q_j \approx q_i$, $q_j - q_i$ tends to be very small. Further, when these particles come in contact, the quantity of charge transferred also tends to be very small. In this limited case, $\Delta q \approx (q_j - q_i)$, so κ_c may be approximated by:

$$\kappa_c = \frac{4\pi r^2}{\Delta A}. \tag{23}$$

Assuming particles are neutralised prior to experimentation, it is reasonable to employ Eq. (23) directly.

If saturation charge data is unavailable, a reasonable approximation of $\Gamma\kappa_c$ for similar, neutralised particles (i.e., $\vec{E}_{\text{contact}} \approx 0$) can be found by rearranging Eq. (16) to:

$$\Gamma\kappa_c = \frac{\Delta q}{\Delta A \varepsilon_0} \tag{24}$$

This expression becomes less accurate as the initial charge is increased since $\vec{E}_{\text{contact}}$ would no longer be negligible.

The value of ΔA is dependent on the mechanical properties of the particle as well as the relative impact velocity of the particle. The value of ΔA may be determined using the DEM. Alternatively, one may also employ experimental data and a Hertzian approximation for the contact area if the material properties and impact velocity are known. For particle-wall contacts:

$$\Delta A_i = 4\pi r_i^2 \left(\frac{5\pi}{128}\rho_i \frac{1-\nu_i^2}{Y_i}\right)^{0.4} \hat{v}_{i,n}^{0.8}, \tag{25}$$

and for particle-particle contacts:

$$\Delta A = \pi \left[\frac{15\sqrt{2}}{32}\frac{m_i m_j}{m_i + m_j}\left(\frac{1-\nu_i^2}{Y_i} + \frac{1-\nu_j^2}{Y_j}\right)\right]^{0.4} \times \left(\frac{2 r_i r_j}{r_i + r_j}\right)^{0.8} \hat{v}_n^{0.8}, \tag{26}$$

where m is the particle mass [9,40,41].

As both Γ and κ_c are based on variable properties, they both will have maximum, minimum and average values. These values can be determined using the maximum, minimum and average values from, for example, the particle radii. In this study, all maxima and minima were evaluated using the upper and lower bounds of 95% confidence intervals of the particle radii, initial charge, charge transfer, and contact area from experimental data.

Fig. 3 presents a flowchart to facilitate the selection of appropriate parameters for various modelling scenarios.

2.3. Electrostatic fields

The final feature of the system to be modelled are the various electrostatic field contributions, i.e, the $\vec{E}_{\text{contact}}$ term in Eq. (16). As electrostatic fields obey the law of superposition, several methods exist to capture the field contributions of all particles in the system, whether in active contact or not. However, not all methods are equal; there is a trade off between computational cost and accuracy. Here, we provide an overview of several methods employed previously in the literature.

The electrostatic field contributions can be broken down into several types, such that:

$$\vec{E}_{\text{contact}} = \vec{E}_{\text{ij}} + \vec{E}_{\text{near}} + \vec{E}_{\text{far}} \tag{27}$$

Here, $\vec{E}_{\text{ij}}$ is the field due to the charges carried by particles i and j in the case of particle-particle contact, or by particle i alone in a particle-wall interaction. $\vec{E}_{\text{ij}}$ is given by Coulomb's Law, where:

$$\vec{E}_{\text{ij}} = \begin{cases} \left(\dfrac{q_j}{4\pi\varepsilon_0 r_j^2} - \dfrac{q_i}{4\pi\varepsilon_0 r_i^2}\right)\hat{r}, & \text{if particle} - \text{particle}, \\ \dfrac{-q_i}{4\pi\varepsilon_0 r_i^2}\hat{r}, & \text{if particle} - \text{wall}, \end{cases} \tag{28}$$

where q is the charge on a given particle, r is that particle's radius, and $\hat{r}$ is the radial unit vector describing the separation of the particle centroids.

The remaining terms are applicable in multi-particle systems only: $\vec{E}_{\text{near}}$ describes the contribution of particles that fall within a user-defined cutoff radius; $\vec{E}_{\text{far}}$ describes those that fall without.

Laurentie et al. [13,14] employed a full pairwise sum (PS) method for all particles within the system, not distinguishing between near and far particles. In this arrangement, the electrostatic field at the centroid of particle i was found by:

$$\vec{E}_i = \frac{1}{4\pi\varepsilon_0} \sum_{k=1,k\neq i}^{n} q_k \frac{\vec{x}_i - \vec{x}_k}{||\vec{x}_i - \vec{x}_k||^3}, \tag{29}$$

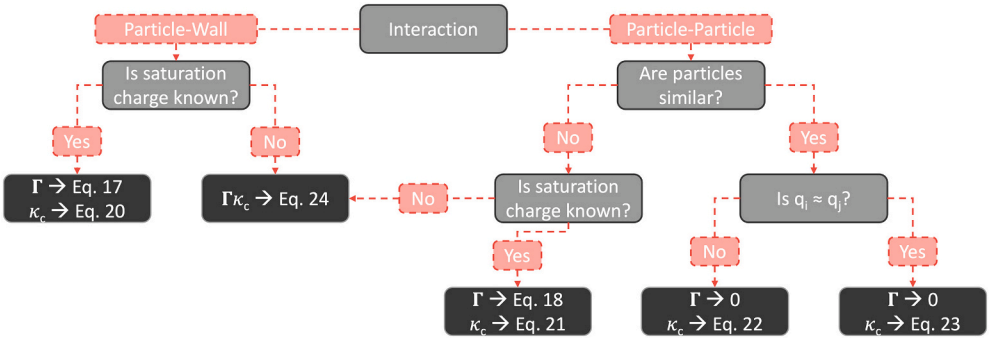

Fig. 3. Flowchart to determine the appropriate charging model parameters based on interaction type and known quantities from experimental data.

where $\vec{x}$ is the position vector of each particle. While this method is the most accurate, it is by far the most computationally expensive, requiring $O(n^2)$ operations to evaluate the contributions from n particles in the domain.

To reduce the computational load, some studies have implemented a direct truncation (DT) method whereby the user-defined cutoff radius, r_{cutoff}, is used to mask the number of particles contributing to the local electrostatic field [15–17,19,20,41]. The electrostatic field is evaluated in the same way as in Eq. (29), with a check to ensure that $||\vec{x}_i - \vec{x}_k|| \leq r_{\text{cutoff}}$. The DT approach is less computationally intensive, requiring $O(n^2_{x_i \leq r_{\text{cutoff}}})$ operations. However, by truncating the contributions of particles outside of r_{cutoff}, accuracy is exchanged for efficiency [19]. Furthermore, Pei et al. found that the DT method was highly sensitive to the chosen cutoff distance [19].

Pei et al. [19] introduced the so-called hybrid particle-cell (HPC) method whereby particles are mapped to a mesh of m computational cells. The net charge within each cell is stored at that cell's centroid. The field contributions are broken down into strong (i.e. "near" particles, $\leq r_{cutoff}$) and weak (i.e. "far" particles, $> r_{cutoff}$) interactions. Both contributions are computed via pairwise sum, however the strong contributions are evaluated from the nearby particles directly whereas the weak are computed from the net charge and position of the cell centroids. This method offers improved computational efficiency, requiring $O(nm)$ operations the cells beyond r_{cutoff}, however it does not consider the influence of physical boundaries on the fields. Pei and colleagues concluded that the HPC method offers improved robustness, accuracy and efficiency relative to the DT method [19].

Kolehmainen et al. [15–17] proposed what is called the hybrid injection method (HIM) for evaluating electrostatic fields. This method maps charges to to cells then solves Poisson's equation for electrostatics. A correction is introduced to avoid double-counting between strong and weak contributions. This approach requires $O(n \log(n))$ operations, offering improved performance over those methods presented previously.

In the HIM, the strong fields are calculated using PS and stored at the particle centroids. Weak interactions are found by first solving Poisson's equation for electrostatics, $\nabla^2\Phi = -\rho_q/\varepsilon_0$, where Φ is the electrical potential and ρ_q is the charge density. Then, the weak field is determined by evaluating the gradient of the potential, as follows:

$$\vec{E}_{\nabla^2} = -\nabla\Phi, \tag{30}$$

using the finite volume method. Here, $\nabla\Phi$ is the gradient of the potential. Dirichlet boundary conditions are employed and set to $0V$ on all surfaces. Under circumstances where two particles are not captured by the same computational cell, a correction is introduced [15–17]:

$$\vec{E}_{\text{cor}} = \frac{-1}{4\pi\varepsilon_0} \sum_{\left|\left|\vec{x}_i - \vec{x}_k\right|\right| \leq r_{\text{cutoff}}} \begin{cases} 0, & \text{if } \vec{x}_{i,\text{cell}} = \vec{x}_{j,\text{cell}}, \\ q_j \dfrac{\vec{x}_{i,\text{cell}} - \vec{x}_{j,\text{cell}}}{\left|\left|\vec{x}_{i,\text{cell}} - \vec{x}_{j,\text{cell}}\right|\right|^3}, & \text{otherwise.} \end{cases} \tag{31}$$

2.4. Implementation

In this work, strong field contributions from particles are evaluated using the PS method. While this is the most computationally intensive approach, it is the most accurate. The number of particles employed here is sufficiently limited to permit its use without marked increases in processing time. However, Kolehmainen et al's. HIM method has also been implemented for use in subsequent investigations with increased complexity in terms of geometry, particle species, and number of particles within the domain.

As the simulation domain being considered is enclosed within a grounded (i.e.,$\Phi_{enclosure} = 0[V]$), conducting boundary, image charges are also considered. The image charges are assumed to have equal, but opposite charge at a distance reflected over the plane of contact. Under circumstances where particles are located near two (or three) boundaries, additional reflections are included to produce balanced quadrupoles (or octapoles). Unlike with real particles, images that fall outside of the cutoff distance are truncated. While this is consistent with the approach of the DT method, the sensitivity of the system to longer-range image interactions was not considered here.

For both the 2D and 3D case, the overall algorithm for modelling triboelectric charging follows that of Laurentie et al. [13,14,29]:

1. Update the particle positions and velocities using the laws of motion.
2. Identify contacting bodies (particles and/or walls).
3. Determine the overlap and evaluate the change in contact area.
4. Find the electrostatic field at the centroid of each particle. If the contact is between two particles, use linear interpolation to find the field at the point of contact. If the contact is between a particle and a wall, calculate the field at the point of contact directly using Eq. (28).
5. Evaluate the quantity of charge exchanged.
6. Determine the electrostatic force acting on each particle.
7. Use the Hertz model to update the mechanical forces and moments.

This algorithm is repeated at each time step over the duration of the simulation time.

3. Model validation: single contact

In this section, we present the results of the preliminary model validation against single particle contacts, and compare the outputs of the 2D and 3D models.

3.1. Single contact – particle-wall

The first contact scenario modelled was the impact of a single particle on a planar surface. The results from both the 2D and 3D simulations were compared against the experimental work reported by Chowdhury et al. [7] and Watanabe et al. [42]. Chowdhury et al. studied the charge transfer from single contacts with a focus on high-density polyethylene (HDPE) and polytetrafluorethylene (PTFE) contacting an aluminium plate [7]. Watanabe et al. studied the charge transferred by single contacts of common pharmaceutical materials against stainless steel, namely: α-lactose monohydrate (αLM), a common excipient; aspirin (ASP), an analgesic; and, sucrose granules (SG), a composite tablet core material [42]. A summary of their respective findings are found in Table 1. Table 1 also summarises the average values of Γ and κ_c for each interaction, calculated using Eqs. (17) and (20). The mechanical properties used in the DEM and to calculate are found in Table 2. The maximum and minimum Γ and κ_c values employed within the model were derived by varying the input parameters within their respective 95% confidence intervals, as described in Section 2.2.

Each model scenario was run 300 times in both 2D and 3D. In all cases, Γ and κ_c were modified every 100 cycles in order to compare the minimum, maximum and average values. Figs. 4 and 5 compare directly the results from 2D and 3D with the published experimental data. The aim of this verification is to ensure that the models reproduce the experimental data for single contacts with good agreement. This test, as well as that for the particle-particle contact model, is intended to ensure the models function as expected.

In all cases, 3D was found to show better agreement with the experimental data. However, the average charge transfer values tended to fall slightly below that of the experimental work. The 2D model was found to underestimate the average charge transfer for the polymers, and overestimate for the pharmaceutical materials; the 2D model's performance was less consistent than 3D's. Furthermore, looking only at the results from the average Γ and κ_c values, the 2D results consistently falls outside of the experimental 95% confidence intervals. The overall charge transfer trends from the 2D and 3D models show very good agreement, both with the experimental data and each other. In terms of speed, the overall processing time of the 2D model was appreciably lower than that of the 3D (seconds versus a few minutes).

In general, the reasonable agreement of the results from both models lend support to the validity of this modelling approach.

3.2. Single contact – particle-particle

Single particle-particle contacts were compared against experimental data collected by Chowdhury et al. [9] for polyamide (PA) 66. In their work, the interaction of free-falling 3.2, 4.0 and 4.8 *mm* particles

Table 2
Summary of the mechanical properties used in the calculation of Γ and for the DEM models.

Particle	Y [GPa]	ν []	ρ [kg/m^3]	μ []	$v_{\widehat{n}}$ [m/s]
PTFE	0.564	0.42	2150	0.065	2.56
HDPE	0.800	0.46	968	0.31	2.56
αLM	18.0	0.3	1540	0.5	4.9
ASP	7.2	0.3	1400	0.5	5.5
SG	23.0	0.21	1581	0.5	4.5

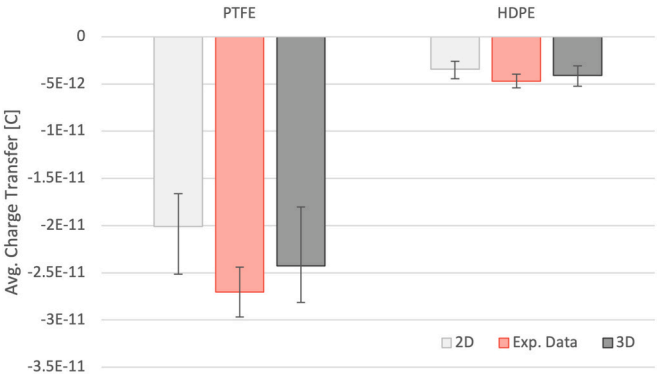

Fig. 4. A comparison of the numerical and experimental results of single particle-wall contact charging behaviour of PTFE and HDPE. The 3D model tended to show better agreement with the experimental data compared to the 2D. The maximum and minimum values for both simulations (error bars) overlap with the experimental 95% confidence intervals.

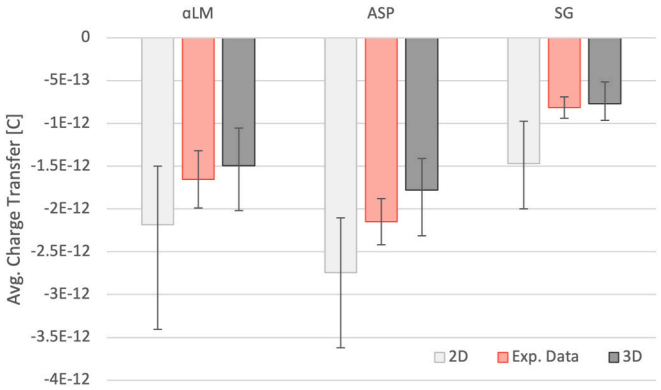

Fig. 5. A comparison of the numerical and experimental results of single particle-wall contact charging behaviour of αLM, ASP and SG. The 3D model continues to show better agreement with the experimental data. The maximum and minimum values for both 2D and 3D simulations (error bars) tend to overlap with the experimental 95% confidence intervals, however the 2D fails to do so for all values in the SG scenario.

Table 1
Summary of the average experimental results from the literature, as well as the corresponding charging model parameters, Γ and κ_c, determined using the published data [7,42].

Particle	Plate	Rad. [mm]	q_i [C]	Δq [C]	q_{sat} [C]	Γ [V/m]	κ_c
PTFE	Al	3.18	−1.71e-10	−2.70e-11	−6.57e-10	−2.34e6	9.64
HDPE	Al	3.18	−3.2e-11	−4.70e-12	−3.97e-10	−1.39e6	3.65
αLM	SS	0.2751,b	2.29e-12	−1.65e-12	−1.81e-11	−2.15e6	36.62
ASP	SS	0.2751,2	−1.37e-12	−2.41e-12	−4.01e-11	−4.77e6	16.45
SG	SS	0.2752	−1.01e-12	−8.16e-13	−1.58e-11	−1.88e6	28.55

Table 3
Summary of the average experimental results from the literature used to evaluate the corresponding charging model parameter, κ_c [9]. The difference in surface charge density, $\Delta\sigma_0$, and the charge transfer, Δq, are assumed to belong to half-normal distributions since the incident and target particle were not specified, nor was the direction of charge transfer.

Particle	Rad. [*mm*]	$\Delta\sigma_0$ [*C*]	Δq [*C*]	κ_c
PA66	3.18	8.02e-13	8.57e-13	27.79
PA66	4.0	4.48e-13	1.09e-12	40.66

were studied in several combinations. As this study focuses on the interaction of like spheres, the model parameters were evaluated from their like particle experiments, namely the 3.18 and 4.0 *mm* experiments. In particle-particle contacts between like particles, Γ tends to zero, hence the only relevant charging model parameter in this case is κ_c. Here, κ_c is determined using Eq. (22). It should be noted that the experimental results taken from Chowdhury et al. for the evaluation of κ_c have been assumed to belong to a half-normal distribution since the incident and target particles were not specified, nor was the direction of charge transfer; these values are summarised in Table 3. The mechanical properties of the particles as implemented in the DEM simulation are found in Table 4.

Following the particle-wall study, each scenario was run 300 times, varying κ_c between the minimum, average and maximum every 100 runs. Fig. 6 presents a comparison of the 2D and 3D model outputs alongside the experimental data from the literature. Once again, the agreement between the 3D model and the experimental data is stronger than that of the 2D. Further, if only the average value of κ_c is considered, the 2D results once again fall outside of the experimental confidence intervals. The overall trends found by both 2D and 3D simulations show good agreement with those of the experimental data. The 2D model outperformed the 3D in terms of speed.

As was found with the particle-wall study, one could expect reasonable order of magnitude charge transfer values from the 2D model, and good indication of charging trends. Again, however, better agreement with experimental data could be found with the 3D model. The reasonable agreement between the results from both the 2D and 3D simulations further support the modelling approach adopted here.

4. Model validation: multi-contact

Multi-contact particle charging was studied in two modes. The first mode looked at the charging behaviour of singular particles coming into repeated contact with a vibrating stainless steel enclosure. The second mode incorporated multiple particles within the same shaking enclosure. Single-particle studies were carried out on PTFE particles with diameters of 3.18, 7.14, 11.11 *mm*. A multi-particle system was investigated using 12.7 *mm* particles.

4.1. Experimental determination of model parameters

A number of different experimental methods may be used for the determination of the charging parameters. As is discussed in the previous section, experimental data published by Chowdhury et al. and Watanabe et al. [7,9,42] was used to determine these parameters for different materials. As an illustration, for particle-wall contacts, both groups used a free-fall set-up with Faraday cages to measure the initial and final charge of particles. Knowing the drop height and material

Table 4
Summary of the mechanical properties used in the particle-particle single contact DEM models.

Particle	Y [*GPa*]	ν []	ρ [kg/m^3]	μ []	v [*m/s*]	θ []
PA66	1.27	0.49	1140	0.26	1.71	0.33

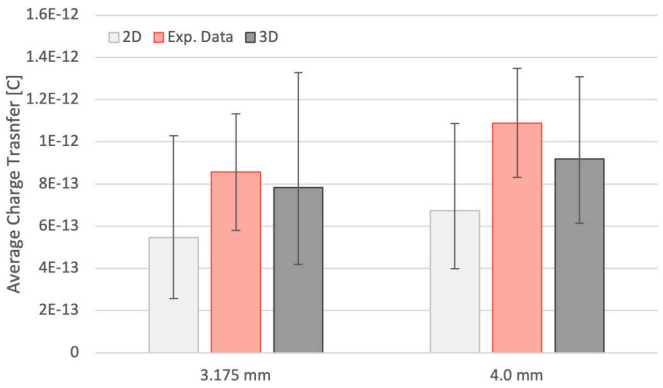

Fig. 6. A comparison of the numerical and experimental results of single particle-particle contact charging behaviour of 3.18 and 4.0 *mm* PA66 particles. As with the particle-wall study described previously, 3D tended to show better agreement compared to 2D. However, there is, once again, a good agreement between the overall trends found by each model.

properties of the contact plate and particle enable the use of Eqs. (26) and (20).

In this study, two experimental methods were used to obtain constants for the DEM simulations and to verify the model outputs. The first, known as the reciprocating charger, was employed to evaluate the model parameters Γ and κ_c. The second, the vibratory shaker, was used to study the saturation charging behaviour. Descriptions of these systems and the associated testing procedures are included here.

4.1.1. Reciprocating charger

A continuous charging/measurement method developed by Cruise et al. [38], combining a Faraday pail with a grounded stainless steel container, was employed (Fig. 7). The Faraday pail comprised a ø60 *mm* by 60 *mm* cylindrical container within a larger (ø85 *mm* by 85 *mm*) container. Both cylinders were insulated from each other by a polyurethane potting compound. A Bayonet Neill-Concelman (BNC) connector was mounted to the side of the outer container. The BNC connector served to ground the outer cylinder whilst providing a connection for the inner cylinder to a Keithley 6517b electrometer. An identical ø60 *mm* by 60 *mm* container was then mounted to the top of the inner cylinder of the Faraday pail. A 2 *mm* polylactide ring was used to electrically insulate the two ø60 *mm* containers. This second container was then grounded. The full system acted as a grounded stainless steel capsule, wherein half of the capsule permitted the measurement of charge. The entire system was then enclosed in a grounded metal cover

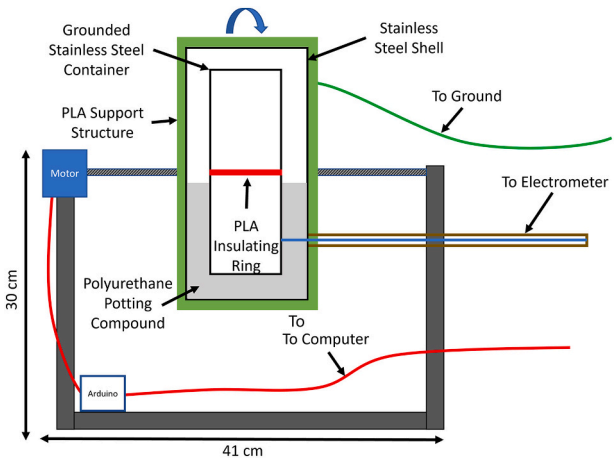

Fig. 7. A diagram describing the construction of the reciprocating charger designed by Cruise et al. [38].

which shielded the charging system from external electromagnetic fields. The charge measurement system was mounted on an axle connected to a servo motor which could rotate the system by 180 °.

To charge and measure the charge transfer to a particle or set of particles, the particles were first cleaned in anhydrous ethanol and allowed to air dry. They were subsequently neutralised using a Simco-Ion MEB neutralising bar. They were then placed into a Faraday pail to measure any remaining charge; while the ioniser was able to effectively reduce the initial surface charge, it was not able to fully neutralise it. The particles were then gently placed in the charging capsule which was sealed and connected to the servo motor. The system was then set to rotate 180 °, wait 2 seconds and then rotate back. In doing so the particles would fall 122 mm onto stainless steel repeatedly, having their charge measured after every 2 contacts. This allowed for the continuous measurement of charge as a function of contact number as it increased up to a saturation point. For the evaluation of Γ and κ_c, 3.18 *mm*, 7.14 *mm* and 11.11 *mm* PTFE spheres were employed.

The reciprocating charger was housed in an environmentally-controlled glove box set to 30 ° *C* and 30% relative humidity.

4.1.2. Vibratory shaker

The vibratory shaker comprised a ø60 *mm* by 60 *mm* container mounted to a speaker driver. The shaker was then attached to a rotating platform connected to a servo motor above a Faraday pail (Fig. 8). Following a charging cycle, the servo would activate and deposit the particle(s) into the Faraday pail to measure the net charge. A 30 *Hz* sinusoidal wave was generated using *f Generator Pro* V6.2.0. The volume was adjusted to produce an amplitude of 1 *mm*, verified via high speed video at 600 frames per second. Single and multiple particles were vibrated for times ranging from 1 to 60 sec. As above, the particles were first cleaned in ethanol and then neutralised using the Simco-Ion MEB bar prior to each run.

The vibratory shaker was used to study the charging behaviour of 12.7 *mm* PTFE particles. This size was employed to test the predictive power of the 2D and 3D DEM models using parameters taken from other particle sizes under different environmental conditions.

All vibratory shaker tests were conducted under ambient laboratory conditions, namely 22–23° *C* and 43–48% relative humidity. A portable dehumidifier was used to maintain the humidity within this range.

4.2. Single particle

The single particle verification was performed in three steps. The first was to determine the charging model parameters from experimental data. The data were collected using the reciprocating charger and three reference particle sizes (3.18, 7.14 and 11.11 *mm*). The values for Γ and κ_c were then evaluated from the data, and are summarised in Table 5.

The second step was to simulate the shaking of each of the reference particles using the charging parameters evaluated from their respective experimental data sets. This was done to ensure that the charging behaviour reported by the model was as expected. Each run simulated 60 seconds of shaking. Good agreement was achieved between the experimental and simulated charge values.

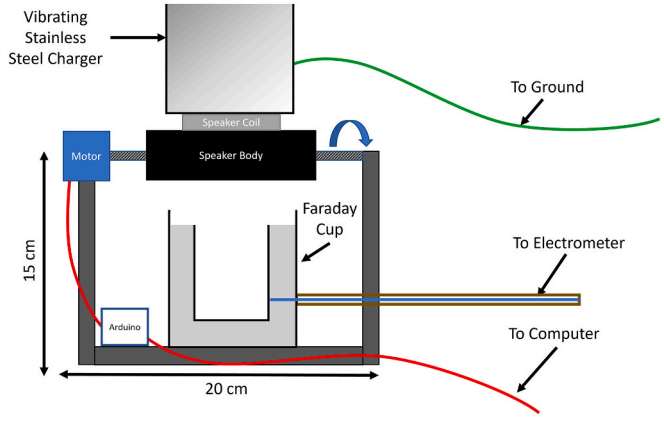

Fig. 8. A diagram describing the construction of the vibratory shaker.

Table 5
Summary of the values of Γ and κ_c evaluated from experimental data. Particle diameter is in [*mm*], Γ in [*V/m*,] and κ_c is dimensionless.

Diam.	Γ_{min}	Γ_{avg}	Γ_{max}	$\kappa_{c,min}$	$\kappa_{c,avg}$	$\kappa_{c,max}$
3.18	−1.44e6	−1.52e6	−1.60e6	17.1	27.2	44.4
7.14	−9.16e5	−9.62e5	−1.01e6	6.1	13.0	34.0
11.11	−7.66e5	−8.03e5	−8.41e5	13.0	19.7	28.1

Table 6
Summary of the predicted values of Γ and κ_c for the 12.7 *mm* particles. Particle diameter is in *mm*, Γ in [*V/m*], and κ_c is dimensionless. The predicted value of κ_c come from the average of the values determined experimentally for the 3.18, 7.14 and 11.11 *mm* particles.

Diam.	Γ_{min}	Γ_{avg}	Γ_{max}	$\kappa_{c,min}$	$\kappa_{c,avg}$	$\kappa_{c,max}$
12.7	−7.32e5	−7.67e5	−8.03e5	12.0	20.0	35.5

The same simulations were re-run using the minimum, average and maximum κ_c values, as κ_c is independent of diameter. These values are summarised in Table 6. Each size class was run 30 times, varying the values of Γ and κ_c from between the minimum, average and maximum every 10 runs. As an illustration, Fig. 9 presents a comparison of the outputs from the 2D and 3D models to the experimental data for an 11.11 *mm* PTFE particle shaken for 60 seconds. While the 2D model tended to produce lower values than the 3D, the agreement with the experimental data for both was generally quite good.

As was found with the single contact studies, the 2D model was appreciably faster than the 3D (several minutes for the 2D simulations versus around an hour for the 3D).

4.3. Multiple particles

For relevance to industrial systems, predictions of charge on multiple particle systems is required. Here, the 2D and 3D models were used to predict the charging behaviour of thirteen 12.7 *mm* PTFE particles shaken for 60 seconds. These results were compared subsequently with experimental data. The 12.7 *mm* particle size was selected because it fell outside of the range of particle sizes used to estimate initially the charging parameters. If the model is capable of predicting the charging behaviour of multiple 12.7 *mm* particles using extrapolated charging parameters, the the model would be considered valid.

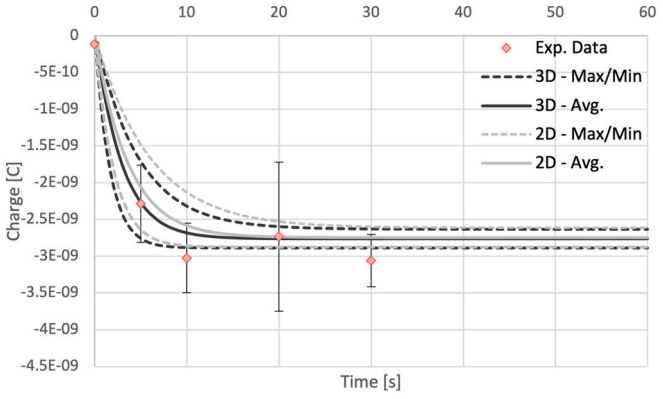

Fig. 9. A comparison of the numerical and experimental results of a single 11.11 *mm* PTFE particle shaken for 60 sec. Both the 2D and 3D models showed good agreement with the experimental data.

The charging parameters were derived from the experimental data described in the previous section. The estimates for Γ and κ_c for for the particle-wall contacts of 12.7 *mm* particles are summarised in Table 6. For particle-particle contacts, κ_c was estimated by Eq. (23). The average contact area, ΔA, was estimated by running a one-second simulation with the thirteen particles in 3D. Over this time, the simulation output the contact area for each particle-particle interaction. These data were then averaged, and the resulting particle-particle κ_c was found to be around 3600.

4.3.1. Saturation charge: limitations in 2D

Fig. 10 presents the predicted bulk charge from both the 2D and 3D models. In this case, the 2D model no longer agreed with the experimental data. In the 2D case, thirteen 12.7 *mm* disks take up approximately 46% of the shaker area, whereas the same number of particles occupy only around 6% of the 3D shaker volume. With such a large disks-to-area ratio in the 2D case, some particles spend little time in contact with the walls. This results in a much wider spread of particle charges since the particle-wall contacts drive the acquisition of negative charge. In Fig. 11, the maximum and minimum individual particle charges from each model are displayed alongside the overall average charge. While the averages show very good agreement with one another, they obscure the individual particle charge contributions. The data spread is clearly greater for the 2D model compared to the 3D.

To correct the discrepancy, the 2D model was re-deployed with four particles instead of thirteen. This number was chosen as a reasonable estimate of the number of particles that could intersect an arbitrary cross-section of the 3D domain at any given time. The minimum and maximum values from this run are once again compared with those from the thirteen particle 3D model in Fig. 12. This adjustment resulted in the spread of charges being constrained similarly to the 3D model. However, it was unable to match the overall average charge. In comparison with the 3D maximum and minimum, there is relatively little change in a particle's charge once it becomes saturated. This oversimplification may, once again, result in poor agreement of more complex models with experimental data.

Considering these limitations, the 2D model is best suited to either simple interactions (e.g., single particles or particle pairs) or for rough order of magnitude performance estimates. Its principal advantage over the 3D model is speed, however for more complex interactions, a trade-off between computational speed and accuracy must be considered.

4.3.2. Prediction of bulk charge

For the experimental verification of the model predictions, the vibratory shaker was employed. Thirteen PTFE particles were used. Each experimental run was performed three times with bulk charge measurements taken at 0, 1, 3, 5, 10, 20, 30 and 60 sec.

Fig. 13 presents the model prediction of the bulk sample charge alongside the experimental data. The agreement between the model and the experimental data is very good. Furthermore, the model was able to accurately predict the saturation charge of the bulk sample from charging parameters that were evaluated from an entirely different experimental set-up. This final test confirms the validity of this modelling approach.

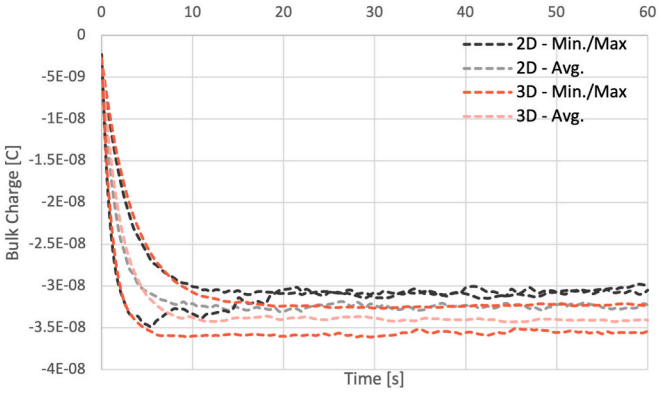

Fig. 10. A comparison of the predicted bulk charge from the 2D and 3D models.

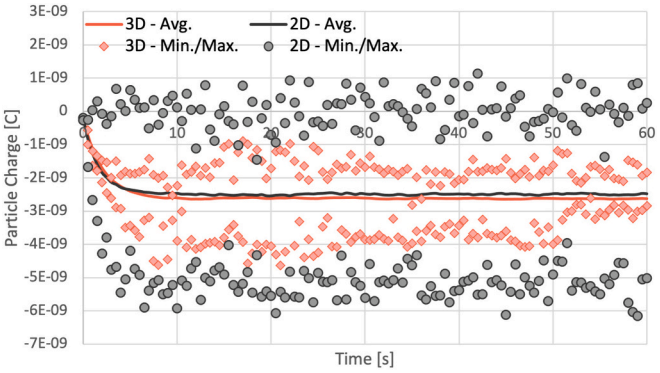

Fig. 11. A comparison of the minimum and maximum particle charges from the 2D and 3D models, as well as the overall average charge. While the averages are quite similar, they obscure the underlying variation in individual particle charge.

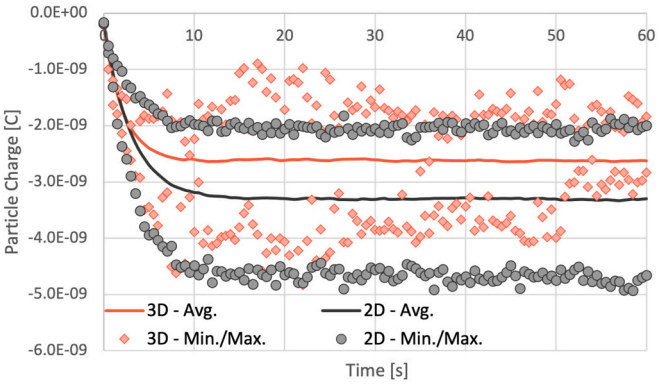

Fig. 12. A comparison of the minimum and maximum particle charges from the four-particle 2D model and the thirteen-particle 3D model, as well as the overall average charge.

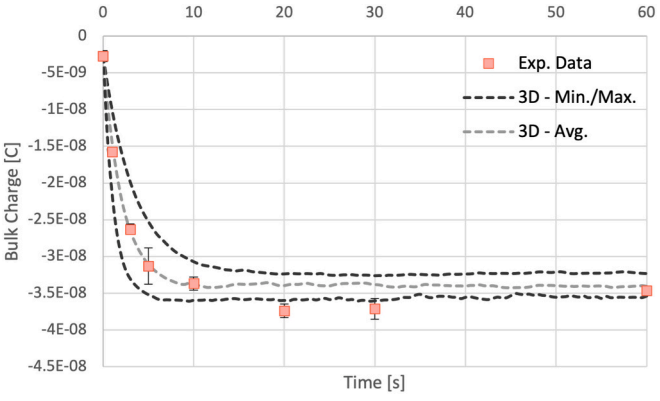

Fig. 13. A comparison thirteen particle 3D model prediction of the bulk sample charge with the experimental data collected. Error bars indicate 95% confidence intervals.

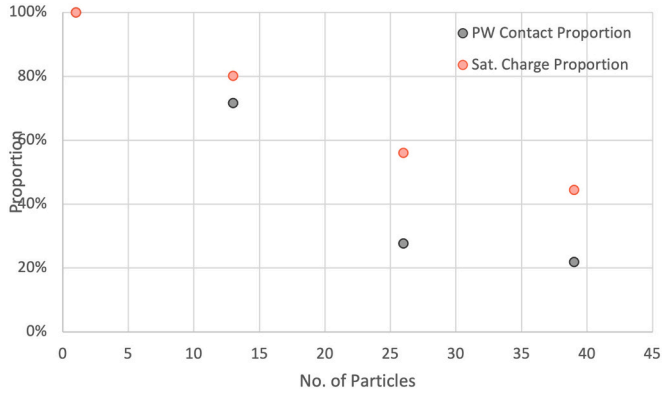

Fig. 14. The relationship between volume fraction, the proportion of particle-wall (PW) contacts, and the proportion of the idealised bulk saturation charge.

4.3.3. *Effect of packing on bulk charge*

The volume fraction of particles within the domain scales linearly with the number of particles. This has an impact on the overall charging behaviour of the system. Specifically, the bulk saturation charge of the particles is inversely proportional to the volume fraction. With a greater volume fraction of particles, the proportion of particle-wall contacts occurring is reduced, assuming all other model parameters remain constant (e.g., shaker amplitude). Thus, the number of particles gaining negative charge from the container walls decreases. As a result, the magnitude of the bulk charge decreases.

An example of these phenomena can be found in Fig. 14. Fig. 14 compares two features against the number of 12.7 *mm* particles in the system: the bulk charge as a percentage of the theoretical bulk charge, and the proportion of the total number of contacts that were between particles and walls. The proportion of the bulk saturation charge was calculated by dividing the overall bulk charge output but the simulation by the 'idealised' bulk charge. The idealised bulk charge is assumed to be the saturation charge of a single particle multiplied by the number of particles in the domain. For example, if a single particle's saturation charge was found to be 1 nC, the idealised bulk charge for 10 particles would be 10 nC. As the volume fraction increases, there is a clear decrease in the overall proportion of particle-wall contacts, and a commensurate decrease in the bulk charge.

5. Conclusions

In this work, an approach to model the tribocharging process is presented alongside a method for the evaluation of key model parameters. The charge modelling method was implemented in 2D and 3D DEM simulations (Matlab and PFC, respectively) and validated against experimental data from both the literature and in-house experimentation. Minor differences were found between the 2D and 3D models for simple particle interaction scenarios (single particle-wall contacts, single particle-particle contacts, and multiple particle-wall contacts of a single particle). In these cases, there was good agreement generally with experimental data. Though the 3D model tended to align more closely with the experimental data, it was inevitably slower.

For more complex, multi-particle, multi-contact systems, the limitations of the 2D model were exposed. The marked increase in packing density resulted in a greater proportion of particle-particle contacts, resulting in a wider spread of individual particle charges. While the average charges found by the 2D and 3D models were similar, they masked the underlying charging behaviour. The 3D model was shown also to be capable of accurate predictions of charging behaviour using model parameters evaluated from different experimental data. Further, the model provided insight to the relationship between volume fraction and bulk saturation charging behaviour.

Modelling of triboelectric effects in industrial systems is challenging, especially when the system contains many unknown or poorly quantified variables. The methods presented in this work for quantifying model parameters are straightforward and effective, and should help to reduce some of the complexity associated with the modelling of triboelectric charging.

Credit Author Statement

J.N. Rasera: Conceptualisation, Computational Methodology and Investigation, Data Analysis, Manuscript Writing, Editing and Revision. **R.D. Cruise:** Experimentation, Experimental Methodology, Data Analysis, Manuscript Writing, Editing and Revision. **J.J. Cilliers:** Supervision, Funding and Resource Acquisition, Manuscript Editing and Revision. **J.-A. Lamamy:** Supervision, Industrial Partner. **K. Hadler:** Supervision, Manuscript Editing and Revision.

Declaration of Competing Interest

The authors declare the following financial interests/personal relationships which may be considered as potential competing interests:J. N. Rasera reports financial support was provided by National Research Fund of Luxembourg. J.N.Rasera reports financial support was provided by Natural Sciences and Engineering Research Council of Canada. J.N. Rasera reports financial support was provided by ispace Europe S.A. J.N. Rasera reports equipment, drugs, or supplies was provided by Itasca Consulting Group, Inc.

Acknowledgements

This research has been made possible through the support of the Luxembourg National Research Fund (FNR) under Industrial Fellowship Grant 12489764.

The authors acknowledge the support of the Natural Sciences and Engineering Research Council of Canada (NSERC) [ref: 411291661]. Cette recherche a été financée par le Conseil de recherches en sciences naturelles et en génie du Canada (CRSNG), [réf: 411291661].

The authors acknowledge the generous support of Itasca Consulting Group for the provision of a PFC license as well as support and mentorship from Dr D.O. Potyondy for J.N. Rasera through the Itasca Educational Partnership Program.

The authors would like to thank Mr S.O. Starr for his valuable feedback and insights.

Finally, the authors acknowledge that this work utilised expertise and prototyping equipment at the Imperial College Advanced Hackspace.

References

[1] S. Trigwell, N. Grable, C.U. Yurteri, R. Sharma, M.K. Mazumder, Effects of surface properties on the tribocharging characteristics of polymer powder as applied to industrial processes, IEEE Trans. Indus. Appl. 39 (1) (2003) 79–86.
[2] L. Xie, N. Bao, Y. Jiang, J. Zhou, Effect of humidity on contact electrification due to collision between spherical particles, AIP Adv. 6 (3) (2016) 035117.
[3] D.J. Lacks, The unpredictability of electrostatic charging, Angew. Chem. Int. Ed. 51 (28) (2012) 6822–6823.
[4] D.J. Lacks, A. Levandovsky, Effect of particle size distribution on the polarity of triboelectric charging in granular insulator systems, J. Electrostat. 65 (2) (2007) 107–112.
[5] S.R. Waitukaitis, V. Lee, J.M. Pierson, S.L. Forman, H.M. Jaeger, Size-dependent same-material tribocharging in insulating grains, Phys. Rev. Lett. 112 (21) (2014) 218001.
[6] H. Zhao, G.P. Castle, I.I. Inculet, A.G. Bailey, Bipolar charging of poly-disperse polymer powders in fluidized beds, IEEE Trans. Indus. Appl. 39 (3) (2003) 612–618.
[7] F. Chowdhury, A. Sowinski, M. Ray, A. Passalacqua, P. Mehrani, Charge generation and saturation on polymer particles due to single and repeated particle-metal contacts, J. Electrostat. 91 (2018) 9–15.
[8] F. Chowdhury, B. Elchamaa, M. Ray, A. Sowinski, A. Passalacqua, P. Mehrani, Apparatus design for measuring electrostatic charge transfer due to particle-particle collisions, Powder Technol. 361 (2020) 860–866.

[9] F. Chowdhury, M. Ray, A. Passalacqua, P. Mehrani, A. Sowinski, Electrostatic charging due to individual particle-particle collisions, Powder Technol. 381 (2021) 352–365.
[10] H. Yu, L. Xie, et al., Numerical simulation of particle size effects on contact electrification in granular systems, J. Electrostat. 90 (2017) 113–122.
[11] L. Xie, G. Li, N. Bao, J. Zhou, Contact electrification by collision of homogenous particles, J. Appl. Phys. 113 (18) (2013) 184908.
[12] W. Hu, L. Xie, X. Zheng, Simulation of the electrification of wind-blown sand, Eur. Phys. J. E 35 (3) (2012) 1–8.
[13] J.-C. Laurentie, P. Traoré, C. Dragan, L. Dascalescu, Numerical modeling of triboelectric charging of granular materials in vibrated beds, in: 2010 IEEE Industry Applications Society Annual Meeting, IEEE, 2010, pp. 1–6.
[14] J. Laurentie, P. Traoré, L. Dascalescu, Discrete element modeling of triboelectric charging of insulating materials in vibrated granular beds, J. Electrostat. 71 (6) (2013) 951–957.
[15] J. Kolehmainen, A. Ozel, C.M. Boyce, S. Sundaresan, A hybrid approach to computing electrostatic forces in fluidized beds of charged particles, AIChE J. 62 (7) (2016) 2282–2295.
[16] J. Kolehmainen, A. Ozel, C.M. Boyce, S. Sundaresan, Triboelectric charging of monodisperse particles in fluidized beds, AIChE J. 63 (6) (2017) 1872–1891.
[17] J. Kolehmainen, P. Sippola, O. Raitanen, A. Ozel, C.M. Boyce, P. Saarenrinne, S. Sundaresan, Effect of humidity on triboelectric charging in a vertically vibrated granular bed: experiments and modeling, Chem. Eng. Sci. 173 (2017) 363–373.
[18] F.S. Ali, M.A. Ali, G. Castle, I. Inculet, Charge Exchange Model of a Disperse System of Spherical Powder Particles, in: Conference Record of 1998 IEEE Industry Applications Conference Thirty-Third IAS Annual Meeting Cat. No. 98CH36242 vol. 3, IEEE, 1998, pp. 1884–1891.
[19] C. Pei, C.-Y. Wu, D. England, S. Byard, H. Berchtold, M. Adams, DEM-CFD modeling of particle systems with long-range electrostatic interactions, AIChE J. 61 (6) (2015) 1792–1803.
[20] P. Sippola, J. Kolehmainen, A. Ozel, X. Liu, P. Saarenrinne, S. Sundaresan, Experimental and numerical study of wall layer development in a tribocharged fluidized bed, J. Fluid Mech. 849 (2018) 860–884.
[21] L. Konopka, J. Kosek, Discrete element modeling of electrostatic charging of polyethylene powder particles, J. Electrostat. 87 (2017) 150–157.
[22] N. Duff, D.J. Lacks, Particle dynamics simulations of triboelectric charging in granular insulator systems, J. Electrostat. 66 (1–2) (2008) 51–57.
[23] K.M. Forward, D.J. Lacks, R.M. Sankaran, Charge segregation depends on particle size in triboelectrically charged granular materials, Phys. Rev. Lett. 102 (2) (2009) 028001.
[24] P.A. Cundall, A computer model for simulating progressive, large-scale movement in blocky rock system, in: Proceedings of the International Symposium on Rock Mechanics, 1971, p. 1971.
[25] P.A. Cundall, O.D. Strack, A discrete numerical model for granular assemblies, geotechnique 29 (1) (1979) 47–65.
[26] L. Schein, M. LaHa, D. Novotny, Theory of insulator charging, Phys. Lett. A 167 (1) (1992) 79–83.
[27] P.A. Cundall, Formulation of a three-dimensional distinct element model-Part I. A scheme to detect and represent contacts in a system composed of many polyhedral blocks, in: International Journal of Rock Mechanics and Mining Sciences & Geomechanics Abstracts vol. 25, Elsevier, 1988, pp. 107–116.
[28] R. Hart, P.A. Cundall, J. Lemos, Formulation of a three-dimensional distinct element model-Part II Mechanical calculations for motion and interaction of a system composed of many polyhedral blocks, in: International journal of rock mechanics and mining sciences & Geomechanics abstracts vol. 25, Elsevier, 1988, pp. 117–125.
[29] I. Itasca, Consulting Group, PFC - Particle Flow Code Ver. 6.0, Itasca Consulting Group, Minneapolis, USA, 2018.
[30] C. Holm, Simulation Methods in Physics 1, Institute for Computational Physics. University of Stuttgart, Stuttgart, Germany, 2013.
[31] S. Naik, S. Sarkar, V. Gupta, B.C. Hancock, Y. Abramov, W. Yu, B. Chaudhuri, A combined experimental and numerical approach to explore tribocharging of pharmaceutical excipients in a hopper chute assembly, Int. J. Pharm. 491 (1–2) (2015) 58–68.
[32] S. Naik, S. Sarkar, B. Hancock, M. Rowland, Y. Abramov, W. Yu, B. Chaudhuri, An experimental and numerical modeling study of tribocharging in pharmaceutical granular mixtures, Powder Technol. 297 (2016) 211–219.
[33] Y. Li, Y. Xu, C. Thornton, A comparison of discrete element simulations and experiments for 'Sandpiles' composed of spherical particles, Powder Technol. 160 (3) (2005) 219–228.
[34] J.M. Boac, M.E. Casada, R.G. Maghirang, J.P. Harner, 3-D and quasi-2-D discrete Element Modeling Of Grain Commingling in a Bucket Elevator Boot System 2010 Pittsburgh, Pennsylvania, American Society of Agricultural and Biological Engineers, Pittsburgh, USA, 2010, p. 2010.
[35] S. Matsusaka, M. Ghadiri, H. Masuda, Electrification of an elastic sphere by repeated impacts on a metal plate, J. Phys. D: Appl. Phys. 33 (18) (2000) 2311.
[36] W.R. Harper, Contact and frictional electrification, Clarendon P., London, UK, 1967.
[37] J. Lowell, A. Rose-Innes, Contact electrification, Adv. Phys. 29 (6) (1980) 947–1023.
[38] R.D. Cruise, K. Hadler, S.O. Starr, J.J. Cilliers, The effect of particle size and relative humidity on triboelectric charge saturation, J. Phys. D: Appl. Phys. (2018), https://doi.org/10.1088/1361-6463/ac5081.
[39] S. Matsusaka, Control of particle tribocharging, KONA Powder Particle J. 29 (2011) 27–38.
[40] M. Ray, F. Chowdhury, A. Sowinski, P. Mehrani, A. Passalacqua, Eulerian modeling of charge transport in bi-disperse particulate flows due to triboelectrification, Phys. Fluids 32 (2) (2020) 023302.
[41] J. Kolehmainen, A. Ozel, S. Sundaresan, Eulerian modelling of gas-solid flows with triboelectric charging, J. Fluid Mech. 848 (2018) 340–369.
[42] H. Watanabe, A. Samimi, Y.L. Ding, M. Ghadiri, T. Matsuyama, K.G. Pitt, Measurement of charge transfer due to single particle impact, Particle & Particle Syst. Character. 23 (2) (2006) 133–137.